IEEE Transactions on Robotics (T-RO) paper presented at
2024 IEEE/RSJ International Conference on Intelligent Robots and Systems (IROS)
October 14-18, 2024. Abu Dhabi, UAE

Multi-modal Soft Amphibious Robots using Simple Plastic Sheet-reinforced Thin Pneumatic Actuators

Jiaxi Wu, Mingxin Wu, Wenhui Chen, Chen Wang, *Senior Member, IEEE*, and Guangming Xie, *Member, IEEE*

***Abstract*—A large challenge in the field of soft amphibious robotics is achieving high maneuverability and multi-terrain adaptability through multi-modal locomotion in hybrid terrestrial-aquatic environments. To address this issue, drawing inspiration from fruit-fly larvae and Spanish dancer sea slugs, a novel tethered soft amphibious robot with multi-modal locomotion is proposed in this paper, performing forward, backward, turning, and self-overturn motions both on land and in water. It leverages plastic sheet-reinforced thin pneumatic actuators, which are constructed from thermoplastic membranes and embedded with a non-stretchable plastic sheet, enabling bi-directional bending with large angles. The robot achieves a forward jumping velocity of 1.77BL/s and a forward swimming velocity of 0.69BL/s, both faster than previously reported soft amphibious robots; connecting two actuator units in parallel, it achieves agile turning with a velocity of 111.8°/s. Our proposed robot demonstrates exceptional multi-terrain adaptability, facile terrestrial-aquatic transition capabilities, and underwater buoyancy adjustment ability. Especially when accidentally overturned, it can recover itself without external assistance, a capability rarely achieved by other soft robots.**

***Index Terms*—soft amphibious robot, multi-modal locomotion, multi-terrain adaptability, thin pneumatic actuator.**

I. Introduction

AFTER millions of years of evolution, organisms have evolved complex and diverse locomotion patterns to move in diverse substrates [1], [2]. For instance, salamanders use their limbs to crawl on land, while swimming by undulating their bodies in water [3], [4]. Frogs effectively use their hind limbs for terrestrial movement via jumping, as well as for aquatic propulsion [5]. Inspired by nature, roboticists have engineered many robots with multi-modal locomotion, especially amphibious robots capable of terrestrial and aquatic movement [6]–[8]. Equipped with multi-modal locomotion, these amphibious robots exhibited exceptional adaptability in hybrid terrestrial-aquatic environments, making them well-suited for environmental monitoring, infrastructure inspection, and disaster response in unstructured scenarios [9], [10]. However, the principles of propulsion on land and in water are fundamentally different, thus some amphibious robots are required to design two distinct propulsive systems or adopt complex transformable structures to accommodate various scenarios [11]–[13]. This typically results in complicated design requirements and intricate switching control schemes between different locomotion systems. Moreover, most of these robots primarily consist of rigid actuation components and hard appearances [14], [15]. This limits their self-adaptability in unstructured environments and poses challenges in interacting with organisms. Particularly when operating underwater, these robots may introduce substantial disturbance to the underwater environment and potentially cause damage upon contact with organisms.

Soft robots are particularly suitable for multi-modal motion on land and in water under a single actuation due to their large deformation capabilities, ease of interaction with the environment, and with no need for intricate transformable mechanisms when transitioning between different motion patterns [16]–[18]. Dong et al. proposed a pneumatic amphibious origami robot with body-sensing ability, capable of executing multi-modal locomotion, including walking, crawling, and swimming [19]. Inspired by tortoises, Wu et al. presented a fully 3D-printed soft amphibious robot and designed six gaits for the robot to enrich its terrain adaptability [20]. Hwang et al. developed an amphibious robot actuated by shape memory alloys (SMA) to mimic terrestrial and aquatic motions of crawling seals [21]. However, existing soft amphibious robots have limitations in their locomotion patterns and maneuverability, making them difficult to fully achieve forward, backward, turning, and self-overturn motions. When overturned by external interference, these robots often become immobilized and require human intervention to resume locomotion. Moreover, they perform limited adaptability to uneven terrains, typically only functioning on flat surfaces, and are hindered when encountering obstacles and steps. Additionally, in aquatic environments, their mobility is largely confined to a specific depth, predominantly the water surface, inhibiting their ability to transition fluidly between the water surface and underwater environments. These aforementioned constraints

This work was supported in part by the National Natural Science Foundation of China under Grants U22A2062, U23B2037, 12272008, and 61973007, and in part by the Beijing Natural Science Foundation under Grant 3242003. *(Corresponding author: Guangming Xie)*

Jiaxi Wu and Mingxin Wu are with the State Key Laboratory for Turbulence and Complex Systems, Intelligent Biomimetic Design Lab, College of Engineering, Peking University, Beijing 100871, China (e-mail: wujiaxi@stu.pku.edu.cn, mingxinwu@stu.pku.edu.cn).

Wenhui Chen is with College of Engineering, Peking University, Beijing 100871, China (e-mail: chenwenhui@stu.pku.edu.cn).

Chen Wang is with the National Engineering Research Center of Software Engineering, Peking University, Beijing 100871, China, and also with the State Key Laboratory for Turbulence and Complex Systems, Intelligent Biomimetic Design Lab, College of Engineering, Peking University, Beijing 100871, China (e-mail: wangchen@pku.edu.cn).

Guangming Xie is with the State Key Laboratory for Turbulence and Complex Systems, Intelligent Biomimetic Design Lab, College of Engineering, Peking University, Beijing 100871, China, and also with the Institute of Ocean Research, Peking University, Beijing 100871, China (e-mail: xiegming@pku.edu.cn).

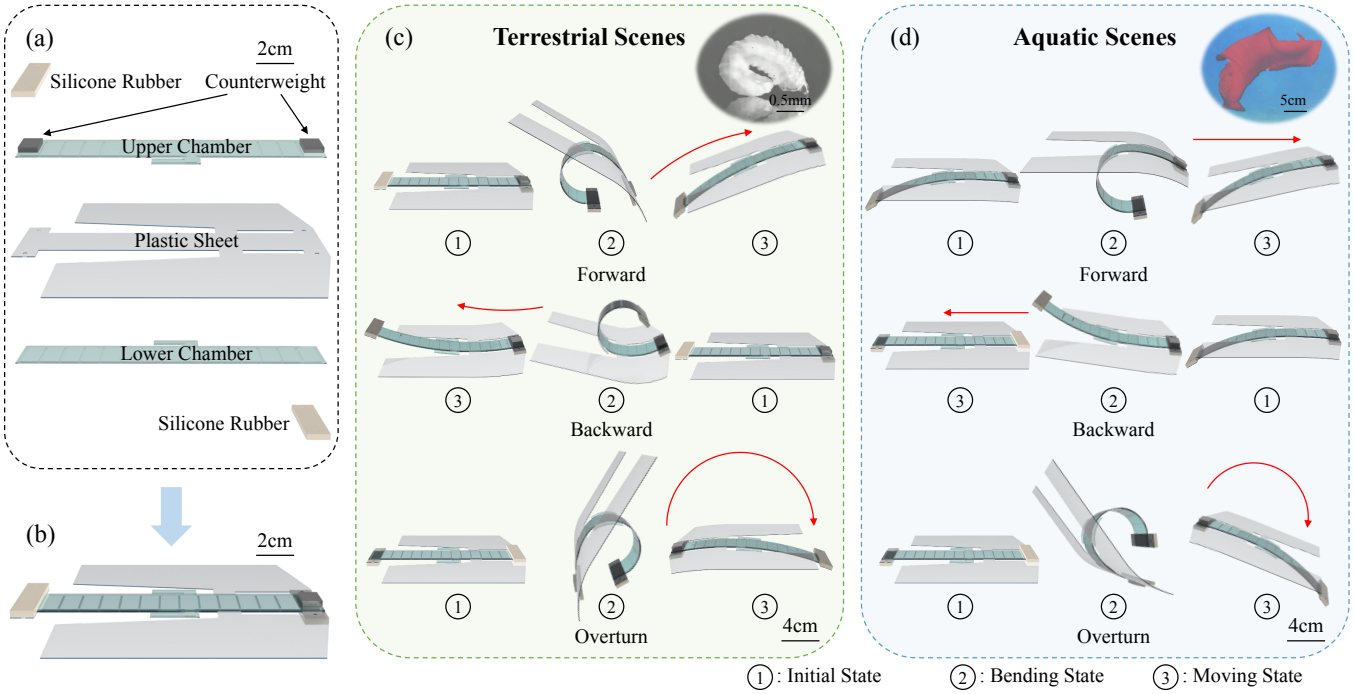

Fig. 1. Design of the soft amphibious robot and motion principle. (a) The robot consists of two thin pneumatic chambers and a semi-rigid plastic sheet. And there are silicone rubbers and counterweights at its head and tail. (b) A CAD rendering of the prototype for the soft amphibious robot. (c) The forward, backward, and overturn motions in terrestrial scenarios. A snapshot of a fruit-fly larva preparing for leaping is in the top right. Reproduced with permission [24]. CopyRight 2019, the Company of Biologists. (d) The forward, backward, and overturn motions in aquatic scenarios. A snapshot of a Spanish dancer sea slug performing swimming is in the top right [27]. Each motion is abstracted into three stages: initial state, bending state, and moving state.

limit their application in dynamic and complex unstructured scenarios.

Fruit-fly larvae typically employ a slow crawling motion as their primary mode of locomotion. However, when confronted with threats, they demonstrate an impressive leaping ability comparable to that of legged jumpers [22], [23]. Fruit-fly larvae store elastic energy by forming their body into a closed loop and contracting their muscles, as shown in Fig. 1(c). Once the loop is released, the stored elastic energy launches them into the air [24]. This mechanism provides them with an effective emergency escape and enables them to overcome obstacles. Similarly, distinct from fish and mammals, there are many soft-bodied animals in the ocean that use different propulsion mechanisms, taking advantage of their flexible bodies. As demonstrated in Fig. 1(d), Spanish dancer sea slugs (*Hexabranchus sanguineus*) propel themselves by pitching their bodies and undulating their large mantles [25], [26]. Ignoring their lateral mantles, their swimming motions can be simplified to alternating patterns of body bending and flattening.

Inspired by the unique locomotion patterns of fruit-fly larvae and Spanish dancer sea slugs, a tethered soft amphibious robot driven by plastic sheet-reinforced thin pneumatic actuators is proposed in this paper to address the limitations of existing soft amphibious robots. The robot primarily moves quickly on land by legless jumping and propels itself in water through periodic bending and flattening of its body. It leverages bi-directional bending thin pneumatic actuators, manufactured by heat drawing of multi-layer thermoplastic membranes [28], [29]. Meanwhile, a semi-rigid plastic sheet is embedded within the actuator to restrict bending shapes and increase output torques. After integrating bilateral fins, our robot is capable of jumping at a velocity of 1.77BL/s and swimming at a velocity of 0.69BL/s, both of which are faster than previously reported soft amphibious robots. Additionally, the robot can perform abundant maneuvers including forward, backward, turning, and self-overturn motions in both terrestrial and aquatic environments, greatly enhancing its mobility in complex and dynamic scenarios. We further demonstrate the robot's locomotion capabilities in uneven environments (slope, obstacle, stair, and gap), various substrates (glass, carpet, sand, mud, and gravel), terrestrial-aquatic transitions, and buoyancy adjustment in water. Overall, the main contributions of this article are as follows:

1) The design and fabrication of the tethered soft amphibious robot leveraging the plastic sheet-reinforced thin pneumatic actuators, achieving faster velocities than existing reported soft amphibious robots.
2) The theoretical analysis to describe the bending behaviors of the actuator with quantitative comparison to experimental tests.
3) The experiment evaluation of the robot with multi-modal locomotion, including forward, backward, turning, and self-overturn motions both on land and in water, which has not yet been fully realized by existing soft robots.
4) The experimental evaluation of the robot for its multi-terrain adaptability, transition capabilities between water and land, and underwater buoyancy adjustment ability.

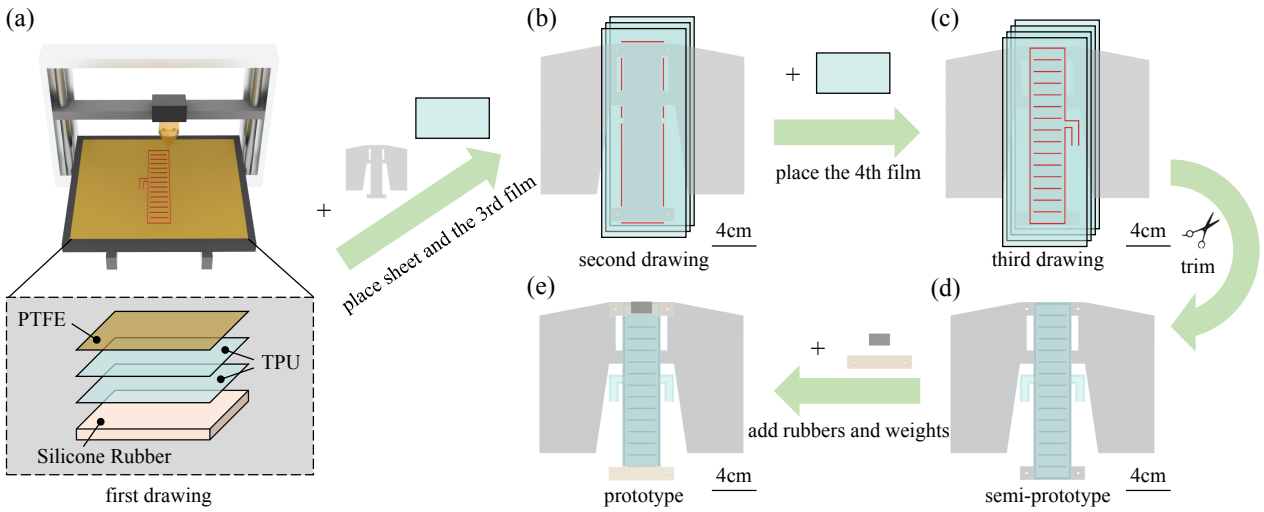

Fig. 2. Fabrication process of the soft amphibious robot. (a) Schematic diagram of the heat drawing using a 3D printer. The heated extruder tip thermally bonds two layers of membranes together to form the upper chamber. (b) Bonding the second and third thermoplastic membranes together and embedding the plastic sheet into the membranes. (c) Sealing the fourth membrane with the third one to create the lower chamber. (d) Trimming the excessive membranes. (e) Attaching two silicone rubbers and two counterweights of 5g to the robot's head and tail to form the prototype.

II. Robot Design and Fabrication

A. System Overview

Drawing inspiration from fruit-fly larvae and Spanish dancer sea slugs, a soft amphibious robot featuring a main body and two lateral fins is designed in this paper, moving through alternating bending and flattening of its main body. The robot is actuated by a four-layer thin pneumatic actuator, with the lower and upper pairs of layers sealed into two separate chambers (upper chamber and lower chamber in Fig. 1(a)). The bending and flattening motions are executed through the collaboration of these two chambers. Distinct from other studies employing thin pneumatic actuators [30], [31], a non-stretchable plastic sheet is embedded between the two chambers, constraining the actuator's bending shape and enhancing its output torque. This plastic sheet also serves to increase energy storage during body bending, facilitating greater jumping distances (JD) following body flattening.

Observation of the bent state of fruit-fly larvae reveals that the curvature of its tail is larger than that of its head, ensuring forward jumping motion [24]. To imitate this feature, a pair of lateral fins is incorporated into the robot's design, constraining its head bending. This ensures the robot's tail fully contacts with the ground during body bending, assisting in a more stable forward jumping. Notably, the lateral fins are integrated with the plastic sheet embedded in the main body for structural simplicity. Furthermore, the robot demonstrates stable forward swimming facilitated by the bilateral fins; without these fins, the robot fails to generate effective forward propulsion, leading to uncontrolled drifting and even capsizing.

B. Fabrication

The thin pneumatic actuators used in this paper are manufactured by heat drawing using a 3D printer (Polarbear S5), capable of producing arbitrary heat sealing curves, as depicted in Fig. 2. The materials used for thin pneumatic actuators and the plastic sheet are thermoplastic urethane (TPU) and polyvinyl chloride (PVC), respectively. We first place two layers of membranes on the 3D printer's plate and utilize a heated extruder tip to thermally bond them together to form the upper chamber (UC). A layer of poly-tetra-fluoroethylene (PTFE) fiber cloth is placed on top of the TPU membranes to avoid sticking between the extruder tip and membranes. Subsequently, a pre-cut PVC sheet and a third TPU membrane are placed on the sealed TPU membranes, and the second and third TPU membranes are bonded together, thus embedding the PVC sheet between them. Afterward, a fourth TPU membrane is placed on top of the third one, sealing it with the third membrane to create the lower chamber (LC). Our method does not require membranes and plastic sheets to be thermally bonded together, allowing for their materials to be freely replaced with other thermoplastic materials and non-stretchable sheets.

After trimming the excessive membranes, two silicone rubbers are attached to the head and tail of the robot to provide sufficient friction for terrestrial propelling. And two counterweights of 5g each are attached to the head and tail to address occasional slipping issues on the ground caused by the robot's relatively lightweight nature. A CAD rendering of the prototype of our proposed soft amphibious robot is depicted in Fig. 1(b). The total weight of the robot is about 31.8g with a size of 16cm$\times$17.6cm$\times$0.8cm.

III. Characterization of the Actuator

The bending characterization of the plastic sheet-reinforced thin pneumatic actuators is explored first. A schematic diagram of the actuator is presented in Fig. 3(a), where each chamber is comprised of six air-interconnected bags and is separated by five seams of width ϵ. The initial state of the actuator with no air is a flat rectangle, while it bends into an arc under positive pressure. More specifically, the membrane chamber inflates into cylindrical surfaces under positive pressure, causing the

embedded plastic sheet to bend into an arc. In this section, if not stated otherwise, the sample size for each physical experiment is n=10. The data are expressed as mean $\pm$ standard deviation.

A. Actuator Modeling

The mathematical model for the thin pneumatic actuators reinforced by an embedded plastic sheet is established based on the virtual work principle. In the following derivation, we assume that (i) the membrane is inextensible, indicating that there is no elastic energy stored in the membrane; (ii) there is no relative displacement between different layers, i.e., there is no energy loss due to friction; and (iii) the airbag length L is much larger than its width W, allowing the surface of the inflated airbag can be considered cylindrical.

The bending of a single airbag is first considered, and a schematic diagram is depicted in Fig. 3(b). Based on Assumptions (i) and (ii), the work of input air is entirely transformed to the unit's moment (torque) M. The energy conservation corresponding to a virtual rotation $\mathrm{d}\theta$ is expressed using the virtual work principle as follows

$$P\mathrm{d}V = M\mathrm{d}\theta \tag{1}$$

where P is the air pressure of the airbag, V is the airbag's volume, and θ is the bending angle of the airbag. Since the Young modulus of PVC sheets is far greater than TPU membranes, the membrane's moment is ignorable as compared to the moment of the embedded plastic sheet. Therefore, considering the plastic sheet as a rectangular cantilever beam, the moment can be represented as

$$M = \frac{\theta EI}{W} = \frac{\theta ELt^3}{12W} \tag{2}$$

where I is the plastic sheet's moment of inertia, E is the Young modulus of the plastic sheet, and t is its thickness.

The bending of the embedded plastic sheet and membranes is approximately a circular arc, then

$$r_1\theta = W \tag{3}$$

$$r_2\phi = W - \epsilon \tag{4}$$

where r_1 is the radius of the curve of the plastic sheet, r_2 is the curve radius of the membrane, ϕ is its corresponding angle,

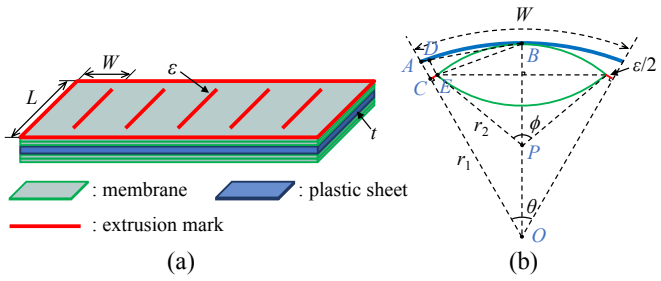

Fig. 3. Modeling of the plastic-sheet reinforced thin pneumatic actuator. (a) Schematic diagram for the actuator, consisting of four TPU membranes and a PVC sheet. (b) Lateral schematic diagram for the bending state of a single airbag.

ϵ is the width of the adhesive part between two membranes. The relationship between θ and ϕ is approximately linear, i.e.,

$$\phi \approx k\theta \tag{5}$$

where k takes the value 2.102 in our case (details is illustrated in Appendix A).

Under Assumption (iii), the volume of the inflated airbag can be represented by

$$\begin{aligned} V &= S \cdot L \\ &= \left(\frac{r_2^2\phi}{4} - \frac{1}{2}r_2^2\cos\frac{\phi}{2}\sin\frac{\phi}{2}\right)\cdot 4 \cdot L \\ &= \left(r_2^2\phi - 2r_2^2\cos\frac{\phi}{2}\sin\frac{\phi}{2}\right)\cdot L \\ &= (\phi - sin\phi)\cdot r_2^2 \cdot L \\ &= \frac{\phi - sin\phi}{\phi^2}\cdot(W-\epsilon)^2 L \end{aligned} \tag{6}$$

where S is the cross-sectional area of the inflated airbag.

Transforming Equation (1) into

$$M = P\frac{\mathrm{d}V}{\mathrm{d}\theta} = P\frac{\mathrm{d}V}{\mathrm{d}\phi}\frac{\mathrm{d}\phi}{\mathrm{d}\theta} \tag{7}$$

Substituting Equations (5) and (6) into the above equation, we can obtain the implicit function between P and θ, i.e.,

$$P\frac{(W-\epsilon)^2}{k^2\theta^3}\left(2\sin(k\theta) - k\theta - k\theta\cos(k\theta)\right) = \frac{\theta Et^3}{12W} \tag{8}$$

For an actuator with n airbags, the entire bending angle Ψ can be represented as

$$\Psi = nc_1\theta(P) \tag{9}$$

where $\theta(P)$ is the mapping from P to θ. Since we ignore the stretchability of TPU and the side surface effect of the airbag, a coefficient c_1=0.46 is introduced into the above equation to correct the difference between the theoretical model and experimental data. And the quantitative comparisons to the experiments are detailed in Section III-C.

B. Simulation Analysis

Subsequently, the deformation of plastic sheet-reinforced thin pneumatic actuators is modeled using finite element analysis (ABAQUS 2022). The hyperelastic property of TPU membranes is characterized through Mooney-Rivlin 5-parameter model

$$\begin{aligned} W =& C_{10}(\bar{I}_1 - 3) + C_{01}(\bar{I}_2 - 3) + C_{20}(\bar{I}_1 - 3)^2 \\ &+ C_{11}(\bar{I}_1 - 3)(\bar{I}_2 - 3) + C_{02}(\bar{I}_2 - 3)^2 + \frac{1}{D_1}(J-1)^2 \end{aligned} \tag{10}$$

where $\bar{I}_1$ is the first strain invariant, $\bar{I}_2$ is the second strain invariant, J is the volumetric strain ratio, and C_{ij} and D_1 are the material parameters. The uniaxial tensile test is tested on Mark-10 F105 for 0.2mm TPU membranes. Five samples of the membranes are pulled at a constant velocity of 200mm/min to about 200% stain change. And the stress-strain curve and the fitted results are shown in Fig. 4.

The geometric model of the actuator is established in ABAQUS 2022 directly. Only half of the actuator is modeled

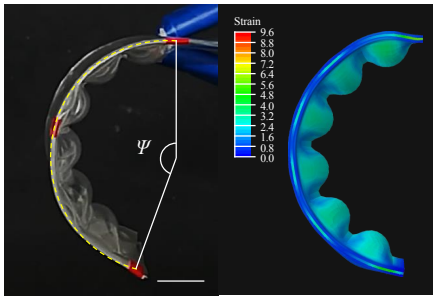

(a)

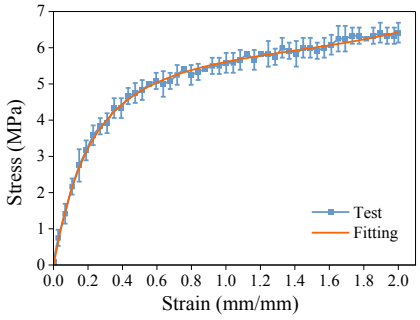

(b)

Hyperelastic material model	Material constant	Value (MPa)
Mooney-Rivlin 5-Parameter Model	C_{10}	-4.710
	C_{01}	9.196
	C_{20}	0.0913
	C_{11}	-0.437
	C_{02}	1.866
	D_1	0

(c)

Fig. 4. Simulation analysis and uniaxial tensile results. (a) Comparison between experimental test and simulated result under 120kPa pressure for the actuator with six airbags. (b) The stress-strain curve obtained by tensile test (sample size n=5). The results are fitted with the Mooney-Rivlin 5-parameter model (red curve). (c) The fitted hyperelastic material parameters. Scale bar, 1cm.

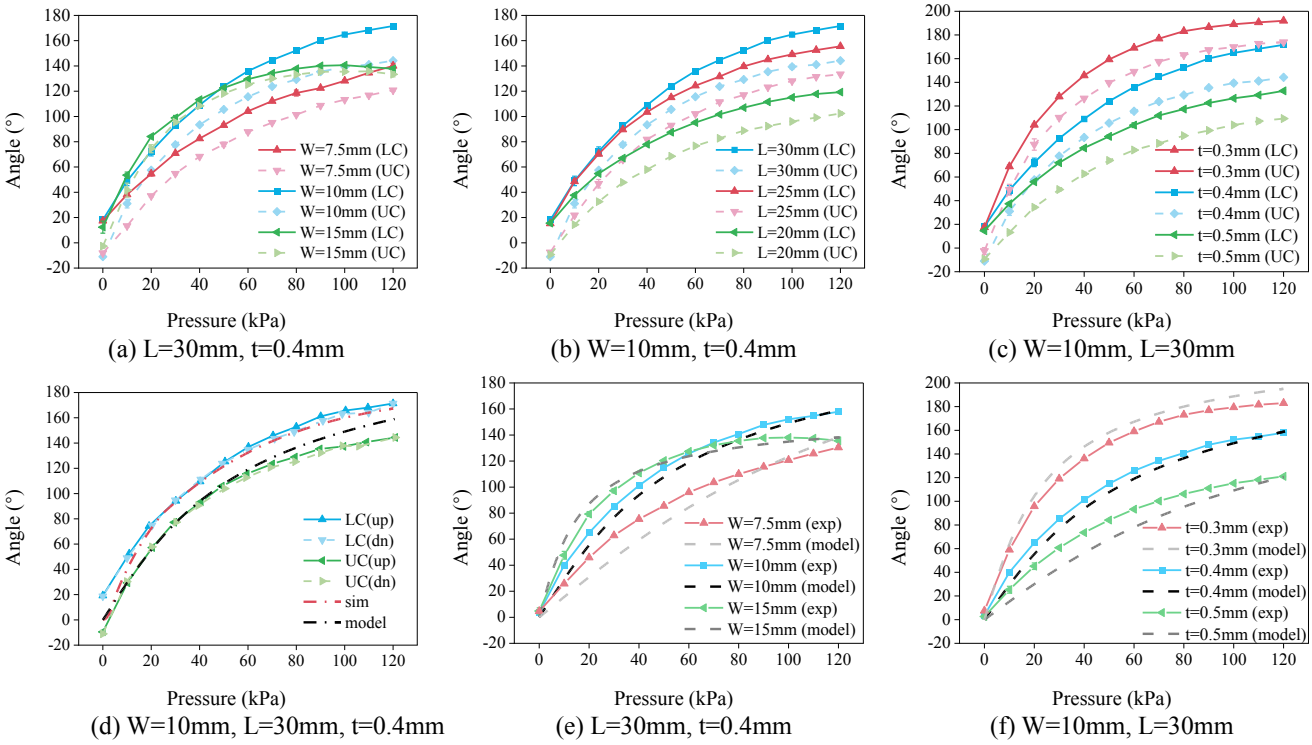

(a) L=30mm, t=0.4mm (b) W=10mm, t=0.4mm (c) W=10mm, L=30mm

(d) W=10mm, L=30mm, t=0.4mm (e) L=30mm, t=0.4mm (f) W=10mm, L=30mm

Fig. 5. Characterization of the thin pneumatic actuators. (a) Relationship of pressure P and bending angle Ψ for the actuator with various airbag widths W. (b) Relationship of pressure P and bending angle Ψ for the actuator with various airbag lengths L. (c) Relationship of pressure P and bending angle Ψ for the actuator with various PVC sheet thicknesses t. (d) Relationship of pressure P and bending angle Ψ, where 'up' means monotonically increasing air pressure, 'dn' means monotonically decreasing air pressure, 'sim' represents the simulated results, and 'model' represents the theoretical model's data. (e) Comparison of analytical model ('model') and experimental test ('exp') with various airbag widths W. (f) Comparison of analytical model ('model') and experimental test ('exp') with various airbag thicknesses t. (sample size n=3 for experimental tests).

using the symmetrical boundary condition to take advantage of its symmetrical shape. Tie constraints are applied to different TPU and PVC layers to mimic the adhesion produced by the 3D printer, while friction contact pairs are defined for the entire surfaces of the actuator to simulate the extrusion-bending deformation and prevent self-penetration. Both TPU and PVC layers are meshed with hexahedrons (C3D8RH) to maximize meshing quality. A positive pressure that increases linearly with time is applied to the inner surface of the upper chamber to characterize the inflation process. A comparison under a pressure of 120kPa is shown in Fig. 4(a). The deformation of the simulation results is basically consistent with the experimental test.

C. Characterization of the Thin Pneumatic Actuator

Furthermore, we compare the performances of actuators with different parameters to explore the influence of the airbag's width W, length L, and thickness t (defined in Fig. 3(a)). It is noteworthy that the actuator's bending angle Ψ is not 0 when no air pressure is applied. This can be attributed to the presence of extrusion marks on one side of the PVC sheet caused by the 3D printer's extruder tip during the third heat drawing. As a result, the thin pneumatic actuator exhibits a certain initial curvature, and the upper and lower chambers of

the actuator are not symmetrical. The bending angle Ψ of the lower chamber is greater than that of the upper chamber under identical pressure conditions. In the bending experiments for different airbag widths (W=7.5/10/15mm, while n=8/6/4 to ensure the entire length remains unchanged), the actuator with W=10mm achieves the largest bending angle at higher pressures (P>50kPa), as shown in Fig. 5(a). When P<50kPa, the actuator with W=15mm exhibits a larger bending angle Ψ; however, the inflated airbags squeeze each other, restricting further bending. More severely, when P>100kPa, the bending angle Ψ decreases with an increase in air pressure P.

The reduction of the actuator's length L results in a decrease in the bending angle Ψ under identical pressure P conditions (Fig. 5(b)). This is because Assumption (iii) in the above model is no longer valid when the length L decreases. Thus the edge effects on both edges cannot be ignored, thereby suppressing the bending of the actuator to some extent. Furthermore, as depicted in Fig. 5(c), an increase in the plastic sheet's thickness t causes a decrease in the bending angle Ψ. A thicker sheet requires more work to bend; thus, under a fixed pressure P, the bending angle Ψ becomes smaller.

Furthermore, we conduct the hysteresis test on the thin pneumatic actuator with W=10mm, L=30mm, and t=0.4mm. The upper and lower chambers are gradually inflated to 120kPa and then deflated slowly. The experimental hysteresis curves are presented in Fig. 5(d). The black dotted line represents the P-Ψ mapping derived from the mathematical model. Since the model ignores the initial bending of the PVC sheet, the model's line is approximately between the practical data of upper and lower chambers. The simulated relationship between applied pressure P and bending angle Ψ is demonstrated as the red dotted line in Fig. 5(d). Although the simulated bending angles are slightly greater than the theoretical model under identical pressures, the overall trends remain consistent. Moreover, the simulated results can basically correspond to the acquired experimental data.

Additionally, as depicted in Fig. 5(e) and (f), parameter sweeps of the analytical model are performed for further comparison with experimental tests. For each airbag width W, the experimental data in Fig. 5(e) are the average bending angles of the upper and lower chambers under identical pressures in Fig. 5(a). The analytical data are calculated by Equation (8) and Equation (9), with only airbag width W varying while keeping other parameters constant, including coefficient c_1. Similarly, the experimental and analytical data in Fig. 5(f) are obtained by the same method. The theoretical model demonstrates a substantial correspondence to experimental tests and basically reflects the changing trend of the bending angle. Especially in Fig. 5(e), the actuator with W=10mm achieves the greatest bending angles under higher pressures, instead of that with W=15mm, which aligns with experimental results. These findings exhibit the model's potential to guide the actuator's design and optimization. However, it is important to acknowledge that there are certain discrepancies between theoretical predictions and experimental data. Therefore, experimental validation is necessary to confirm the actuator's performance.

D. Characterization of the Embedded Plastic Sheet

We next explore the effect of the embedded plastic sheet in the pneumatic actuator. As shown in Fig. 6(a), the bending shapes of the thin pneumatic actuators are restricted by the embedding of the plastic sheet. This semi-rigid sheet stores elastic energy when its body bends, assisting the robot in jumping farther during the flattening state, and the robot incorporating a 0.4mm embedded plastic sheet achieves the farthest jumping distance with 99% test of significance, as illustrated in Fig. 6(c). Although a thicker plastic sheet can store more elastic potential energy, the bending angle of the actuator with thickness t=0.5mm is insufficient to guarantee that the rubber sheet at the robot's tail fully contacts the ground, thus inhibiting its full performance potential. In contrast, under the premise of ensuring sufficient bending, the robot equipped with a 0.4mm embedded plastic sheet stores more elastic potential energy, enabling it to jump farther than robots with plastic sheets of other thicknesses.

Meanwhile, the integration of the bilateral fins limits the bending of the robot's head and ensures its tail fully touches the ground during bending, assisting it to jump forward more

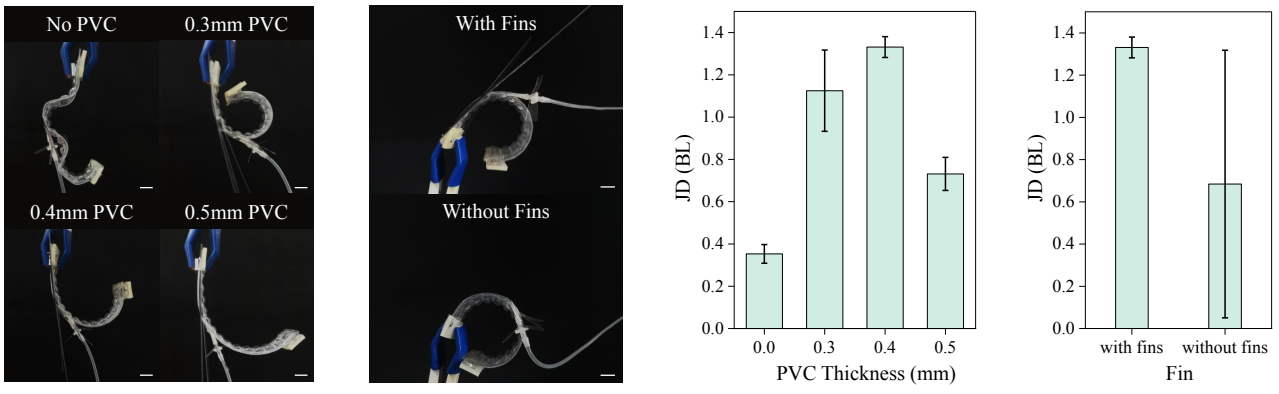

Fig. 6. Characterization of the embedded plastic sheet. (a) Comparison of the robot embedding the PVC sheets with different thicknesses under 80kPa pressure. (b) Comparison of the robot with or without lateral fins under 80kPa pressure. (c) Jumping distances of the robot with 0-0.5mm PVC sheets. (I) Jumping distances of the robot with or without lateral fins. Scale bar, 1cm.

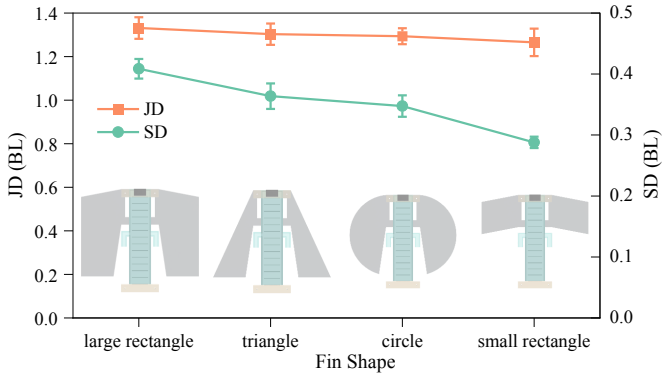

Fig. 7. Jumping and swimming distances of the robot with different fin shapes under a single actuation.

steadily. As demonstrated in Fig. 6(b), without the lateral fins, the bending postures of the head and tail are indistinguishable, resulting in an uncertain locomotion direction. Given the same control sequence, the robot sometimes moves forward and sometimes backward, leading to a large standard deviation in its jumping distance, as presented in Fig. 6(d). Simultaneously, we evaluate the effects of different lateral fin shapes (Fig. 7). While only modest differences are observed in jumping distance on land, the robot equipped with large rectangular fins (first column in Fig. 7) achieves a greater swimming distance (SD) with 99% test of statistical significance compared to those outfitted with alternative fin configurations under identical control sequences. It is speculated that when swimming on the water surface, larger lateral fins provide sufficient water surface tension to keep the front half of the robot floating on the water surface, facilitating a more efficient conversion of the tail's flapping motion into forward propulsion.

According to the preceding discussion, the actuator with W=10mm, L=30mm is capable of greater bending angles under identical pressures. And a 0.4mm plastic sheet can store more elastic potential energy when bending, enabling the robot to jump farther than that with a 0.3mm sheet (with 99% test of significance), and the stiffness of thicker plastic sheets enhances the robot's jumping stability (small standard deviation in Fig. 6(c)). Consequently, in the following sections, the actuator parameters of the soft amphibious robot are determined as W=10mm, L=30mm, and t=0.4mm, and the large rectangle in Fig. 7 is chosen as the robot's fin shape.

IV. Experimental Results

A. Experiment Setups

The control and actuation system of the robot is shown in Fig. 8. The micro control unit (MCU) of the control system is STM32RCT6, which generates PWM signals to regulate the solenoid valves, thereby controlling the connection and disconnection of the air path. MCU receives commands from the computer via Bluetooth to switch between different motion modes. The working voltages of the solenoid valves and the air pump are both 12V, and they are driven by NMOS FQD60N03. The actuation circuit is isolated from the control circuit through optocouplers LTV217.

In order to generate the air-keeping state for terrestrial jumping, all the solenoid valves are configured as two-position two-way, which maintain an open-air path when triggered by an external signal and a closed path in the absence of signals. Two solenoid valves are utilized to regulate the airflow of a chamber, with one for the air-inflating path (the black arrow in Fig. 8(a)), and the other for the air-deflating path (the blue arrow in Fig. 8(a)). When both solenoid valves are closed, the air pressure in the chamber remains constant, preserving the bending shape of the actuator. Consequently, a total of eight solenoid valves are employed to control the dual-body robot with four independent chambers.

The motion of the amphibious robot is recorded using a top-view camera. Subsequently, the motion videos are analyzed by frame to extract the motion trajectories and velocities. The robot covers distances of approximately 800mm and 600mm on land and in water, respectively, in order to calculate velocities for each control sequence (Fig. 9(a)). During the land steering test, the robot completes a rotation of approximately 180° under various control sequences to calculate the corresponding velocities. All control sequences are tested three times, and the resulting data are reported as mean ± standard deviation.

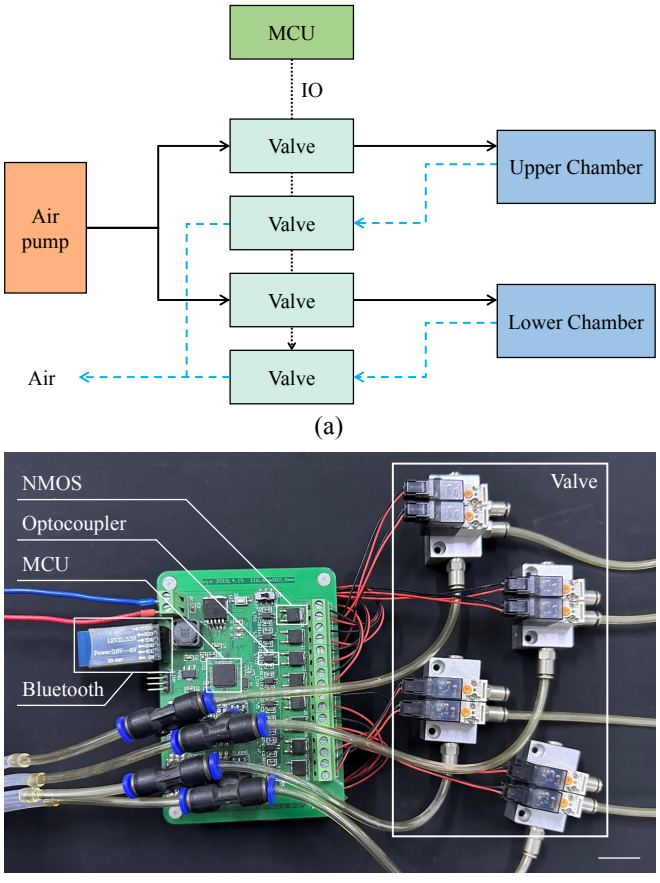

Fig. 8. Control and actuation system for the soft amphibious robot. (a) Schematic diagram. (b) Physical picture. Scale bar, 2cm.

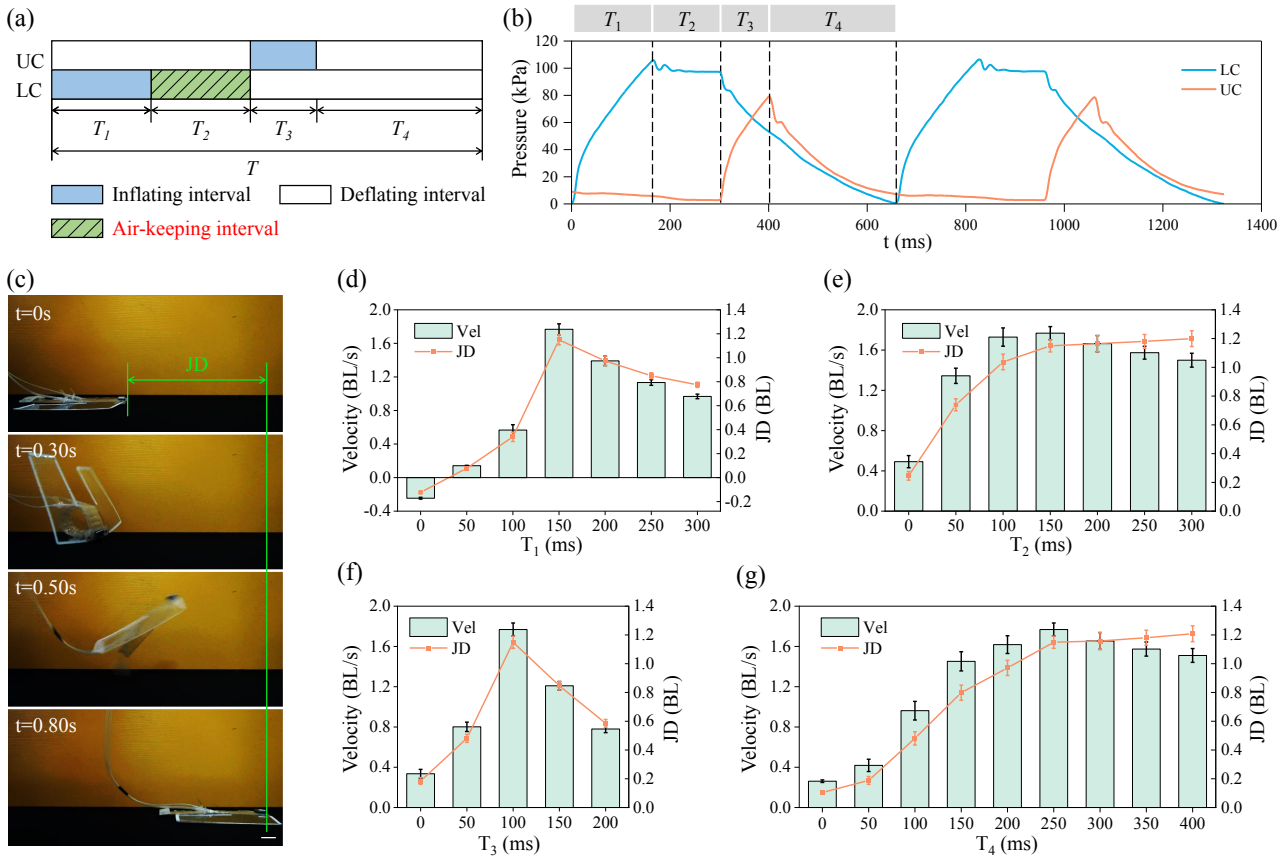

Fig. 9. Terrestrial directional locomotion. (a) Control sequence diagram for terrestrial directional jumping, consisting of four intervals T_1-T_4, where the air-keeping interval T_2 is capable of stabilizing the bending state and increasing the jumping distance. (b) Input air pressures of the two chambers during the terrestrial forward motion. (c) Snapshots of the amphibious robot jumping. (d) Average jumping velocities and jumping distances under the control sequence T=[T_1, 150, 100, 250]ms. (e) Average jumping velocities and jumping distances under the control sequence T=[150, T_2, 100, 250]ms. (f) Average jumping velocities and jumping distances under the control sequence T=[150, 150, T_3, 250]ms. (g) Average jumping velocities and jumping distances under the control sequence T=[150, 150, 100, T_4]ms. Scale bar, 2cm.

B. Terrestrial Locomotion Performance

The proposed amphibious robot primarily travels terrestrially via jumping, achieving much faster velocities than crawling or walking methods employed by other soft robots [19], [21]. The control sequence diagram of terrestrial jumping is depicted in Fig. 9(a), where T_1 represents the inflating interval for the lower chamber, T_3 represents the inflating interval for the upper chamber, and T_4 represents the full deflating interval for both chambers. Notably, there is an interval T_2 between T_1 and T_3, denoting the air-keeping interval for the lower chamber. Introducing T_2 helps stabilize the robot in its bending state and increases the average jumping distance. Fig. 9(b) illustrates the air pressure changing curves of the upper and lower chambers under the control sequence defined in Fig. 9(a).

An entire jumping process is demonstrated in Fig. 9(c). Initially, the robot inflates its lower chamber, causing its body to bend into a ring shape. Due to the integrated lateral fins, the bent ring is not perfectly symmetrical. The curvature of the tail is larger than that of its head, allowing the tail to fully touch the ground, while the head remains approximately perpendicular to the ground, similar to the bent posture of fruit-fly larvae. The lower chamber is then deflated while the upper chamber is inflated, causing the robot's bent body to rapidly flatten and release the stored elastic energy, propelling it forward. Repeating the aforementioned process enables the robot to continuously jump forward.

The robot achieves a maximum forward jumping velocity of 1.77BL/s under the control sequence T=[150, 150, 100, 250]ms (∼1.54Hz), over 1.8 times faster than the reported fastest soft amphibious robot [20]. Interestingly, as shown in Fig. 9(d), when the inflating interval T_1 for the lower chamber is reduced to 0, the robot begins moving backward instead. It is speculated that inflating the upper chamber and bending the robot's body upwards abruptly changes the robot's center of mass, causing it to move backward.

Incorporating an air-keeping interval T_2 into the control sequence increased the average jumping distance (with 99% test of significance), as illustrated in Fig. 9(e). Since the air generated by the air pump is turbulent, the robot cannot ensure that its tail fully contacts the ground during rapid bending. The air-keeping interval T_2 helps stabilize the robot's bending state, allowing its tail to fully touch the ground and maximizing its jumping capability. However, integrating the interval T_2 reduces the control frequency. Thus, a trade-off between control frequency and jumping distance is necessary to pursue the maximum forward jumping velocity.

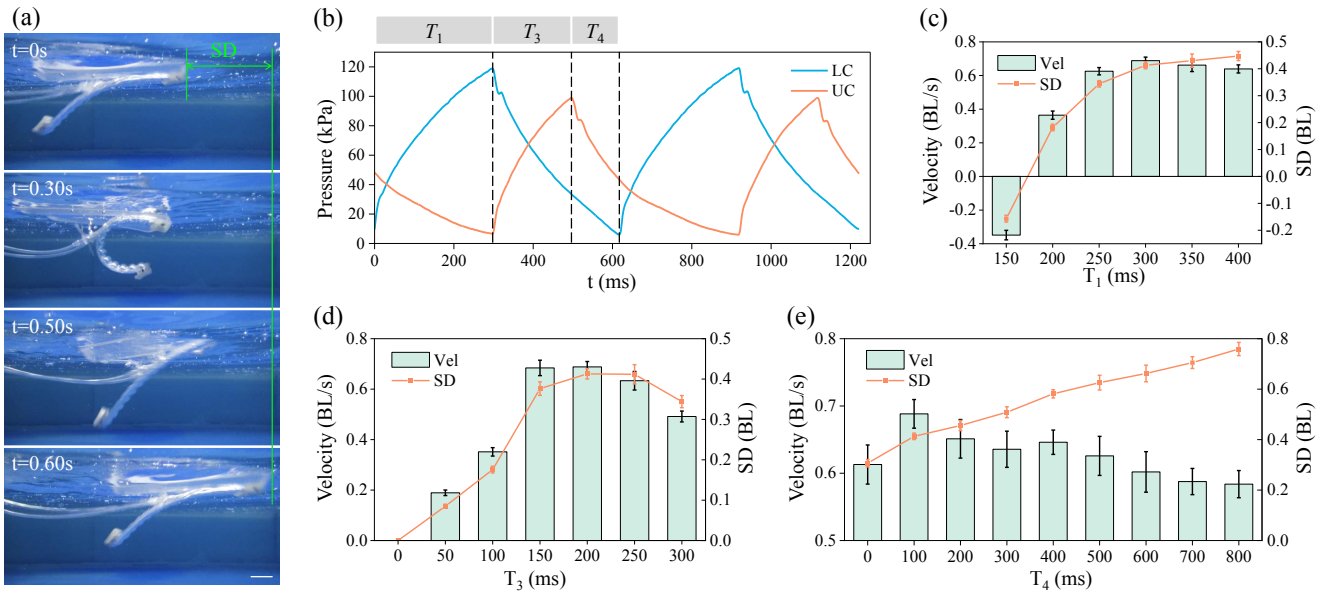

Fig. 10. Aquatic directional locomotion. (a) Snapshots of the amphibious robot swimming. (b) Input air pressures of the two chambers during the aquatic forward motion. (c) Average swimming velocities and swimming distances under the control sequence T=[T_1, 0, 200, 100]ms. (d) Average swimming velocities and swimming distances under the control sequence T=[300, 0, T_3, 100]ms. (e) Average swimming velocities and swimming distances under the control sequence T=[300, 0, 200, T_4]ms. Scale bar, 2cm.

C. Aquatic Locomotion Performance

In addition to terrestrial jumping, the robot is capable of aquatic movement through periodical tail bending and flattening, as demonstrated in Fig. 10(a). This swimming method is similar to that of Spanish dancer sea slugs, which swim through regular body pitching [26]. Unlike the terrestrial control sequence, the robot involves only three phases (T_1, T_3, T_4) during aquatic locomotion. The definitions of T_1, T_3, and T_4 are the same as previously mentioned. Input air pressures of the robot's upper and lower chambers during the aquatic forward motion is illustrated in Fig. 10(b). During the experiments, it is found that the air-keeping interval T_2 is useless for the robot's swimming; therefore, T_2 is removed from the control sequence in aquatic locomotion. The robot achieves a maximum forward swimming velocity of 0.69BL/s with the control sequence T=[300, 200, 100]ms (∼1.67Hz), approximately 2.1 times faster than the reported fastest soft amphibious robot [32]. Similar to terrestrial locomotion, the robot exhibits the ability to swim backward in water when the inflating interval T_1 is small (T_1<T_3), as depicted in the first column of Fig. 10(c). In this case, the robot exhibits an undulating swimming pattern, reminiscent of the undulations of Spanish dancer sea slugs' large mantles [26].

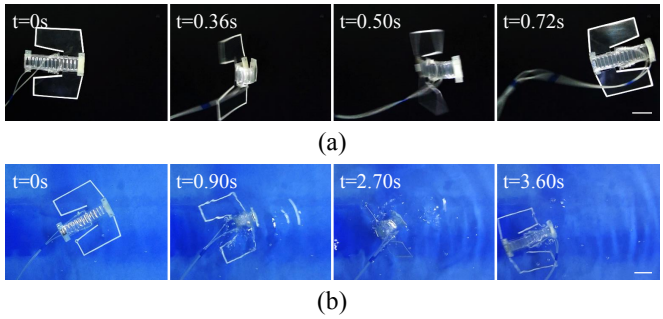

Fig. 11. Self-overturn motions of the amphibious robot (a) on land and (b) in water. Scale bar, 5cm.

Furthermore, when the robot is accidentally overturned, whether on land or in water, it can autonomously self-overturn under modulated control sequences, without any external assistance, a capability rarely achieved by other soft robots (Fig. 11). The robot is capable of rapidly and substantially raising its tail while on land, thereby altering the position of its center of mass and utilizing inertia to accomplish a turnover. Meanwhile, when capsized in aquatic environments, the robot can turn itself completely by repeatedly flapping its tail. In practical scenarios, it is likely for the robot to capsize because of external disturbance, affecting task execution. In such circumstances, the self-overturn ability of our robot is vitally important, further enhancing the robot's maneuverability and broadening its potential application scenarios.

Additionally, the cost of transport (CoT) is measured for both terrestrial and aquatic locomotion. The CoT serves as a metric for evaluating the energy efficiency of locomotion and is represented by

$$\mathrm{CoT} = \frac{P}{mgv} \tag{11}$$

where P is the average power, m is the mass of the robot, g is the gravitational acceleration, and v is the robot's velocity. The CoT of the robot on land is about 24.9 under the control sequence T=[150, 150, 100, 250]ms; and the CoT in water is about 68.3 under the control sequence T=[300, 0, 200, 100]ms.

D. Turning Ability of the Dual-body Robot

Turning ability is crucial for a robot to navigate in unstructured environments; nonetheless, the aforementioned robot primarily achieved directional forward and backward locomotion. To address this issue, two thin pneumatic actuators

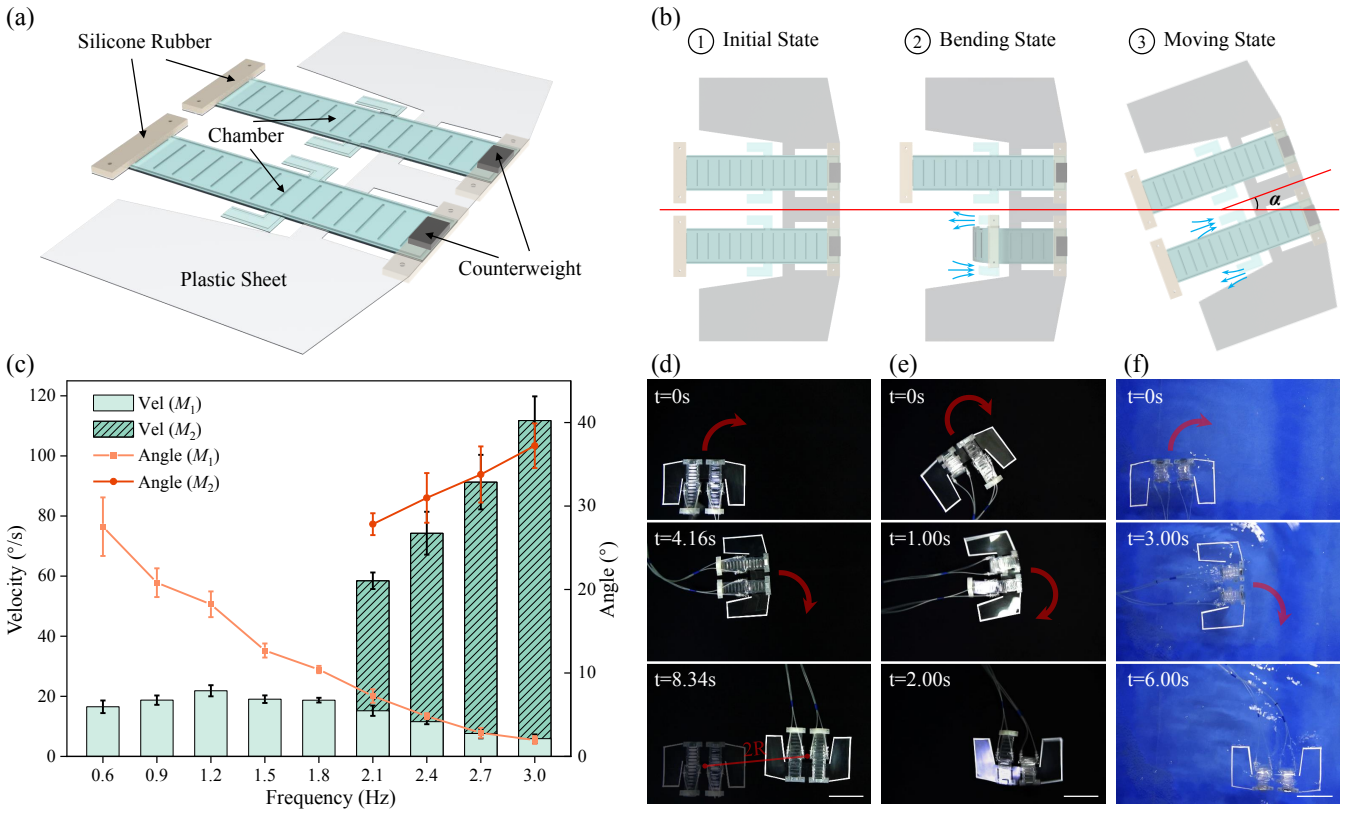

Fig. 12. Turning ability of the dual-body robot. (a) Prototype of the dual-body amphibious robot. (b) Schematic diagram of the dual-body robot turning process. Only one side's chamber of the robot is actuated, thus the robot rotates an angle α to the other side. (c) Comparison of two terrestrial turning mechanisms under various control frequencies. 'Angle' represents the average turning angles for each jumping. (d) Snapshots of the first turning mechanism M_1 on land. The turning radius R is defined in the third picture. (e) Snapshots of the second turning mechanism M_2 on land. (f) Snapshots of the aquatic turning mechanism. Scale bar, 10cm.

are connected in parallel via the embedded plastic sheet, as demonstrated in Fig. 12(a). The robot exhibits agile turning behavior when only a single-side actuator is driven, whereas it performs forward motion under dual-side actuation. Interestingly, it is discovered that the robot employs two turning mechanisms on land. The first mechanism (M_1) involves performing a complete jumping per motion cycle, i.e., one side of the body transitions from extension to curling up and then fully extends, while the other side remains unactuated, as depicted in Fig. 12(b). This first turning strategy is slower, and the turning angle per cycle decreases with the increase of the control frequency, making it more suitable for fine-tuning the moving direction. It achieves a maximum turning velocity of 21.9°/s, with a turning radius of 16.9cm (defined in Fig. 12(d)).

Additionally, the robot possesses a faster turning mechanism (M_2) better suited for emergency steering (Fig. 12(e)). If the robot pre-curls the actuated side of its body into a bent state, lifting its head off the ground, and maintains the bent state throughout the entire jumping cycle (the other side keeps an unactuated flat state), it can turn at the velocity of 111.8°/s (turning radius 6.7cm), significantly faster than the first mechanism with 99% test of significance. It is worth noting that this turning mechanism can only be achieved under high-frequency actuation; otherwise, the robot may fall forward, significantly reducing turning velocity and gradually degenerating into the first mechanism. Details of the control sequences in the terrestrial turning experiments are presented in Appendix B.

Furthermore, the robot is capable of agile aquatic turning, achieving a maximum turning velocity of 30.8°/s with a turning radius of 15.0cm (Fig. 12(f)). Although the aquatic turning mechanism is similar to that on land, involving turning under single-side actuation, it is advantageous for the robot to pre-curl the other side of its body into a ring shape and maintain this posture throughout the turning cycle in aquatic scenarios. This approach reduces the turning radius and enhances the robot's maneuverability in water.

E. Multi-terrain Adaptability

Multiple terrain adaptability is one of the core performance indicators for amphibious robots, allowing them to perform inspection and reconnaissance tasks in complex and ever-changing unstructured environments. Both single-body and dual-body amphibious robots are adaptive to multiple terrains encountered in complex scenarios, as demonstrated in Fig. 13-15. The single-body robot is capable of (1) climbing up a slope of 20°, (2) jumping across a 25mm-high obstacle, (3) jumping up a single step with 25mm height, and (4) climbing continuous stairs (15mm high per step). Furthermore, distinct from the aforementioned gaits, the robot can traverse a 25mm-high gap by wriggling its body like a worm (Fig. 13(e)).

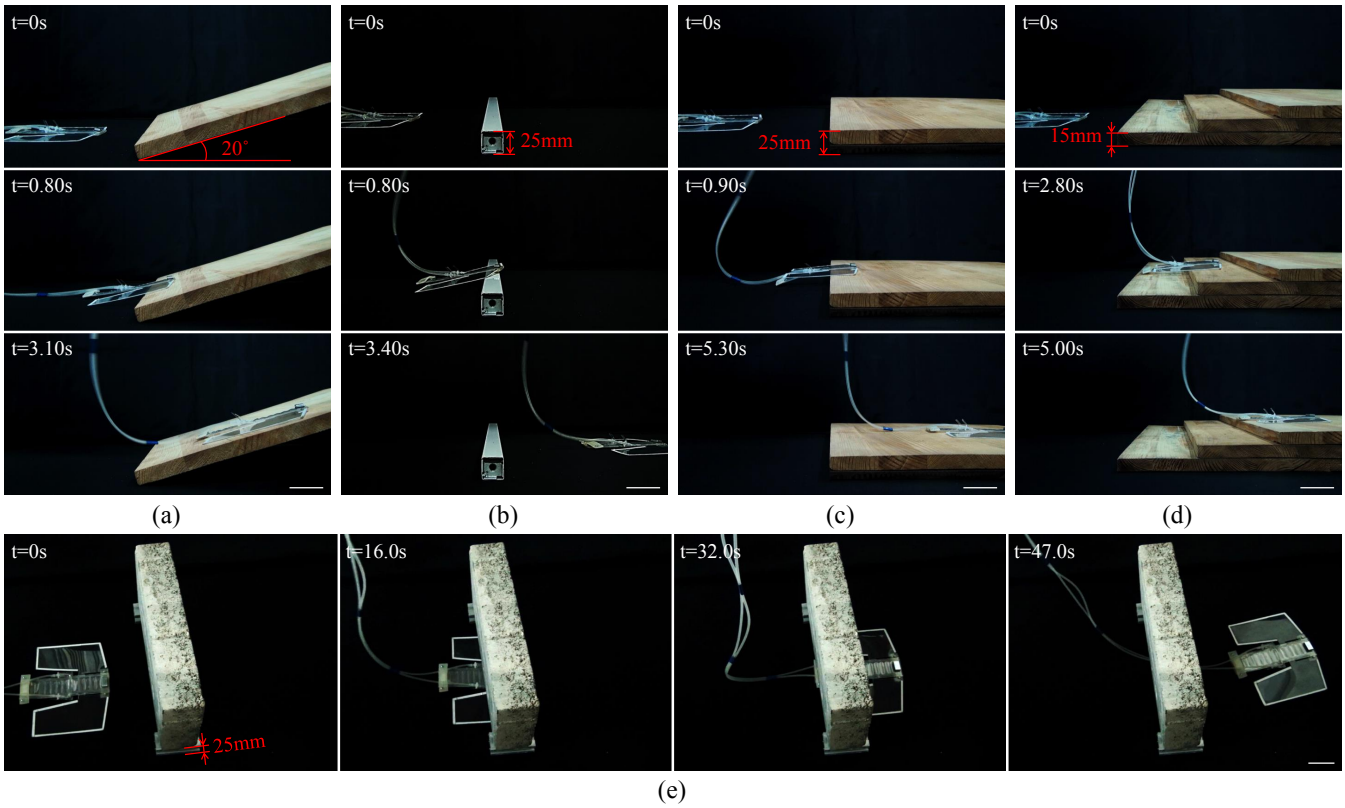

Fig. 13. Multi-terrain adaptability of the soft amphibious robot. (a) Climbing up a slope of 20°. (b) Jumping across a 25mm-high obstacle. (c) Jumping up a single step with 25mm height. (d) Climbing continuous stairs (15mm high per step). (e) Traversing a 25mm-high gap by wriggling its body like a worm. Control sequence details under multiple terrains are presented in Appendix B. Scale bar, 5cm.

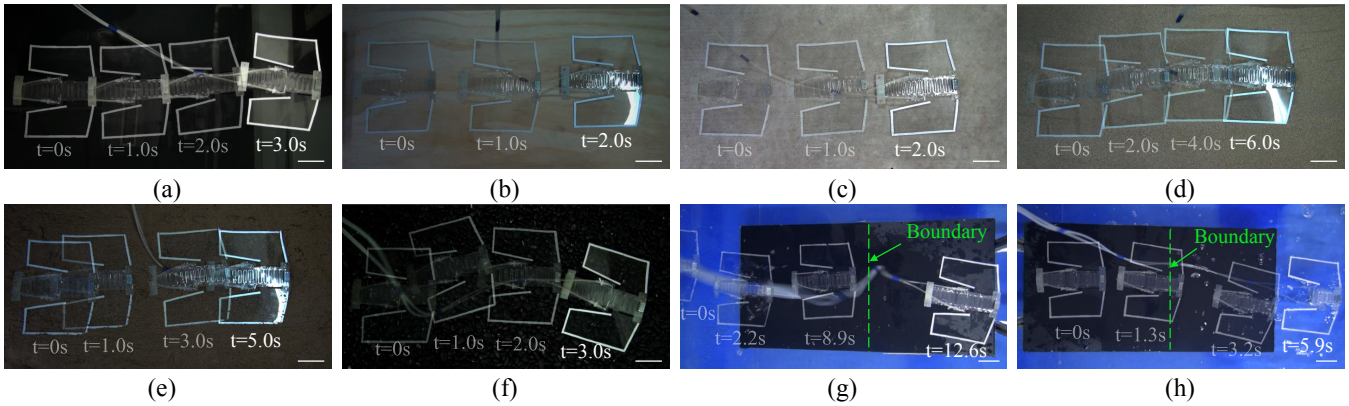

Fig. 14. Adaptive locomotion of the robot on various substrates, including (a) glass, (b) wood, (c) carpet, (d) sand, (e) mud, and (f) gravel. (g) Transition process from water to land. (h) Transition process from land to water. Control sequence details under various substrates are presented in Appendix B. Scale bar, 5cm.

In practical reconnaissance tasks, amphibious robots encounter a wide variety of substrates, making their ability to traverse different surfaces crucial. Our amphibious robot is able to quickly jump across both smooth glass surfaces and rough carpets, regardless of the substrate's friction. Additionally, it can easily traverse uneven and changeable substrates, such as sand, mud, and gravel, which are typically challenging terrains for most soft robots to navigate (Fig. 14). Furthermore, the robot has the ability to swiftly switch between swimming and jumping gaits, enabling smooth transitions from aquatic to terrestrial environments and vice versa.

By combining two actuator units together, the dual-body exhibits agile turning ability, thereby endowing it with the capability to effectively navigate around insurmountable obstacles. The dual-body actuation cooperation allows our robot to navigate as a Ω-shaped path and avoid obstacles in both terrestrial and aquatic environments, as demonstrated in Fig. 15(a) and (b). Moreover, the amphibious robot possesses a unique capability to adjust its own buoyancy by altering the inflation rate. This feature enables it to transition between underwater and surface scenarios, a capability rarely achieved by other soft amphibious robots. When encountering obsta-

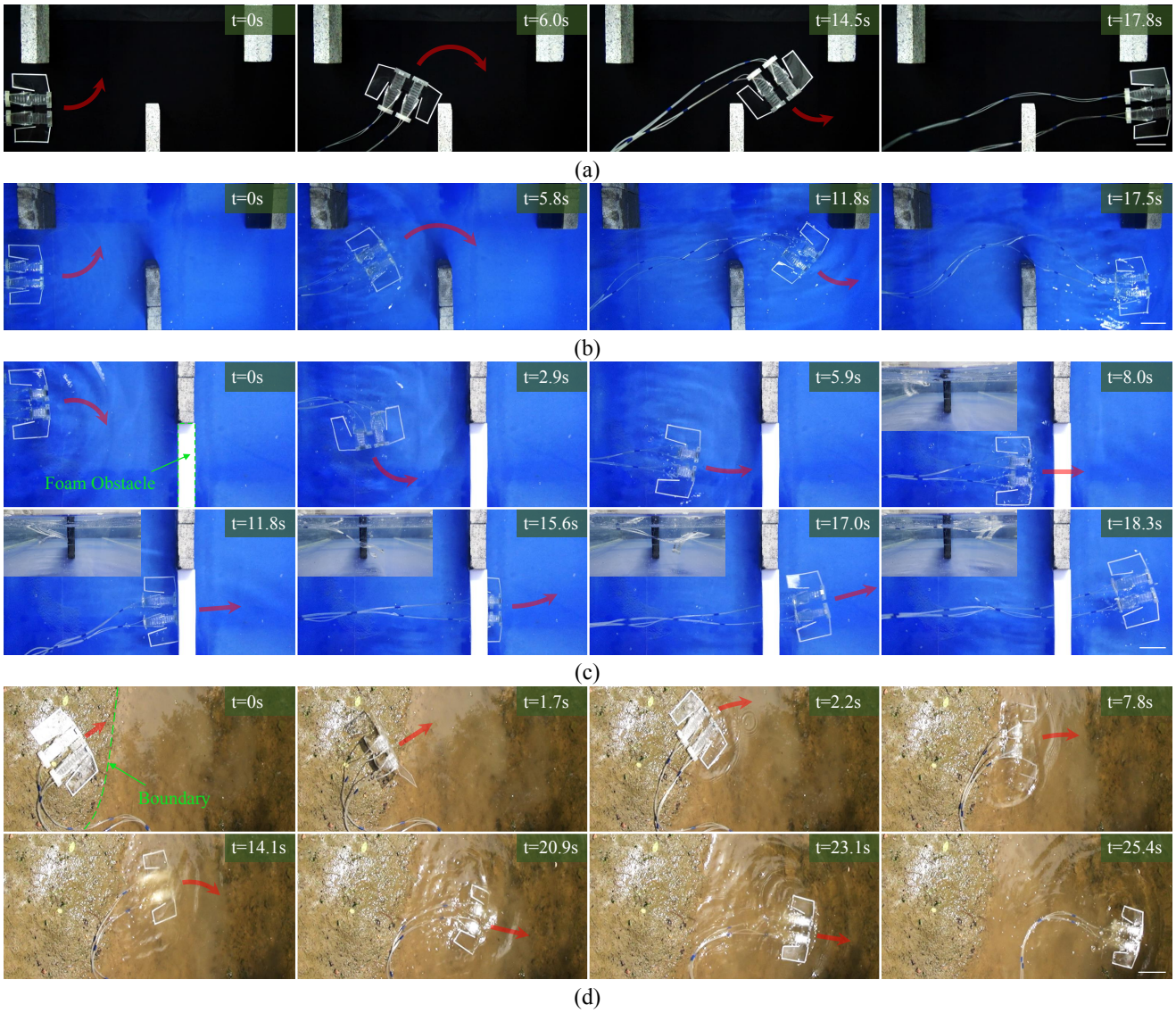

Fig. 15. Obstacle avoidance of the dual-body robot in (a) terrestrial scenarios and (b) aquatic scenarios. (c) Transitions between underwater and surface scenarios by buoyancy adjustment. Snapshots in the top left are the lateral views of the robot's motion. (d) Terrestrial-aquatic transition of the dual-body robot in practical scenarios. Scale bar, 10cm.

cles on the water surface, like buoy foam boards, the robot can dive underwater to circumvent the obstacles and then resurface to continue its progress (Fig. 15(c)). Additionally, we demonstrate the terrestrial-aquatic transition of our robot in a practical river, which is particularly difficult for existing soft amphibious robots (Fig. 15(d)). The robot effectively traverses the muddy terrain, seamlessly transitions into the water, precisely adjusts its orientation, and finally swims off into the distance. Overall, the combination of dual-body actuation and buoyancy adjustment renders our amphibious robot highly versatile and adaptable to a wide range of substrates and terrains, enhancing its potential to perform reconnaissance and inspection tasks in complex and dynamic scenarios.

V. Discussion and Conclusion

In this paper, we present a novel soft amphibious robot capable of continuous jumping and swimming, demonstrating exceptional adaptability to multiple terrains and substrates. Inspired by fruit-fly larvae and Spanish dancer sea slugs, the robot propels itself through the elastic energy released during alternating patterns of body bending and flattening. It leverages plastic sheet-reinforced thin pneumatic actuation, which enables bi-directional bending with large angles. The economical actuators, constructed from thermoplastic membranes and non-stretchable plastic sheets, are manufactured by a 3D printer, ensuring high production accuracy, rapid manufacturing, and repeatability. This combination of soft membranes and semi-rigid plastic sheets equips the robot with the necessary flexibility and strength for performing continuous jumping and swimming gaits. Through alternately bending and flattening its body, our proposed robot achieves terrestrial jumping at a velocity of 1.77BL/s and aquatic swimming at a velocity of 0.69BL/s, both surpassing the reported fastest soft amphibious robots [20], [32] (Table I).

TABLE I
COMPARISON BETWEEN OUR WORK AND EXISTING SOFT AMPHIBIOUS ROBOTS.

	Terrestrial Scenes		Aquatic Scenes		Terrain Adaptability	Amphibious Transitions
	v_F (BL/s)	v_T (°/s)	v_F (BL/s)	v_T (°/s)		
Ours	**1.77**	**111.8**	**0.69**	**30.8**	**Slope, obstacle, stair, gap, glass, carpet, sand, mud, gravel**	**Water→land, land→water**
Patel et al. [18]	0.07	Not given	0.06	Not given	Flat surface	Land→water
Dong et al. [19]	0.025	Not given	0.11	Not given	Flat surface	No
Wu et al. [20]	0.97	25.4	Not given	Not given	Slope, hill, gap, sand, mud, gravel	Water→land
Hwang et al. [21]	0.0091	0.46	0.073	6.1	Flat surface	Land→water
Jin et al. [32]	0.35	Not given	0.33	Not given	Flat surface	No
Zhang et al. [33]	0.11	Unable	Not given	Unable	Smooth surface, vertical wall	No
Milana et al. [34]	0.033	Not given	0.05	Not given	Flat surface	No
Paschal et al. [35]*	0.027	25	Not given	Not given	Flat surface	No
Li et al. [36]*	0.34	Not given	0.040	Not given	Flat surface	No
Tang et al. [37]	0.26	Unable	Not given	Unable	Smooth and semi-smooth surfaces	No
Faudzi et al. [38]	0.27	Not given	0.10	Not given	Slope, sand	No

1. v_F represents the forward velocity, and v_T represents the turning velocity.
2. '*' represents the robot is untethered.

TABLE II
MANEUVERABILITY COMPARISON BETWEEN OUR WORK AND SOME EXISTING SOFT ROBOTS.

	Terrestrial Scenes				Aquatic Scenes			
	Forward	Backward	Turning	Overturn	Forward	Backward	Turning	Overturn
Ours	✔	✔	✔	✔	✔	✔	✔	✔
Patel et al. [18]	✓		✓		✓		✓	✓
Dong et al. [19]	✓		✓		✓		✓	
Hwang et al. [21]	✓		✓		✓		✓	
Zhang et al. [33]	✓	✓			✓	✓		
Drotman et al. [39]	✓	✓	✓					
Chen et al. [40]	✓		✓					
Wang et al. [41]					✓	✓	✓	
Lee et al. [42]					✓		✓	

Meanwhile, the robot can perform various maneuvers through modulating control sequences of the actuator's individual chambers, enabling a comprehensive range of motion rarely fully accomplished by existing soft terrestrial and aquatic robots (Table II). These maneuvers include forward and backward, agile turning, and self-overturn motions in both terrestrial and aquatic environments, allowing the robot to effectively navigate through diverse environments. Among these motion modes, the robot's self-overturn capability is particularly noteworthy, significantly enhancing its overall maneuverability. This unique feature allows the robot to autonomously recover from an overturned position without any external assistance, ensuring uninterrupted task execution even in the face of unexpected disturbances or challenges. Consequently, the versatility of the robot's multi-modal motion enables it to successfully perform tasks in complex scenarios and under external disturbances.

A notable aspect of our soft amphibious robot is its multi-terrain adaptability, allowing it to perform well in a variety of challenging environments. The single-body robot demonstrates impressive capabilities, such as climbing slopes, jumping over obstacles, and ascending stairs, while also exhibiting the ability to traverse gaps by wriggling. Meanwhile, the robot is capable of efficiently traversing smooth glass surfaces, rough carpets, and even more challenging substrates like sand, mud, and gravel. And the swift switch between jumping and swimming gaits allows it to achieve transitions between terrestrial and aquatic environments, addressing a challenge that has often plagued soft amphibious robots. Furthermore, its ability to adjust its own buoyancy enables it to transition between underwater and surface scenarios, further expanding its reachable range. By connecting two actuators in parallel, we have demonstrated that a robot based on such a combination of minimum actuator units can not only maintain the directional motion characteristics of the smallest unit, but also obtain agile steering ability and effectively navigate around insurmountable obstacles. More complex combinations can also be explored to achieve more functions.

In conclusion, the innovative soft amphibious robot presented in this paper exhibits remarkable performance in both terrestrial and aquatic locomotion. It demonstrates versatile locomotion strategies, exceptional multi-terrain adaptability, facile transition capabilities, and the ability to adjust its buoyancy. These characteristics greatly enhance the robot's maneuverability, making it highly suitable for tasks in complex and dynamic environments. Unlike rigid robots, our soft amphibious robot has the advantage of actively or passively changing its shape to adapt to the surrounding environment, making it suitable for navigating in rough and confined spaces. Meanwhile, its inherent flexibility makes it more organism-friendly. In scenarios involving frequent interactions with living entities, our robot can leverage its flexibility to minimize potential harm or damage. In the future, by combining advanced sensors and control algorithms, the robot can perform objective detection, trajectory tracking, and autonomous navigation for intricate scenarios. These integrations will enable the robot to adapt

and respond effectively to various environmental conditions, further improving its functionality and utility in practical environments, especially in unmanned or human-unfriendly circumstances.

Despite the aforementioned advantages, our soft amphibious robot is still improvable. Currently, the robot's functionality depends on tethered pneumatic actuation. However, untethering is essential for amphibious robots' further applications in large environments. The following two aspects will be considered in our future research. One is to integrate the pneumatic actuation systems into the robot. To minimize any adverse effects on the robot's flexibility, these electronics and power components will be encapsulated in silicone. The second is to explore alternative actuation methods, such as light control, to achieve remote power and control, allowing the robot's body to maintain entire compliance. Meanwhile, we briefly discuss the influence of the lateral fin's shapes in this paper. Future work may include conducting a systematic study of various design parameters, such as body geometric characteristics and actuator arrangement, to identify optimal configurations that maximize the robot's locomotion efficiency in various terrestrial and aquatic environments.

ACKNOWLEDGMENTS

The authors thank Dr. Junzheng Zheng in Tsinghua University for his support in ABAQUS simulation.

APPENDIX A

Relationship of θ and ϕ

As illustrated in Fig. 3(b), since $\triangle OAB$ is an isosceles triangle, it can be obtained that

$$\angle OBA = \angle OAB = \frac{\pi}{2} - \frac{\theta}{4} \tag{12}$$

$$AB = 2r_1 \sin\frac{\theta}{4} \tag{13}$$

Similarly,

$$\angle PBE = \angle PEB = \frac{\pi}{2} - \frac{\phi}{4} \tag{14}$$

$$BE = 2r_2 \sin\frac{\phi}{4} \tag{15}$$

Making an auxiliary line DE parallel to AB, then

$$\angle BDE = \angle OAB = \frac{\pi}{2} - \frac{\theta}{4} \tag{16}$$

$$\angle BED = \pi - \angle BDE - \angle DBE = \frac{\pi}{2} + \frac{\theta}{2} - \frac{\phi}{4} \tag{17}$$

$$AD = \frac{CE}{\sin\angle OAB} = \frac{\epsilon/2}{\sin(\pi/2 - \theta/4)} = \frac{\epsilon/2}{\cos(\theta/4)} \tag{18}$$

In $\triangle BDE$, according to the law of sines,

$$\frac{BE}{\angle BDE} = \frac{BD}{\angle BED} = \frac{AB - AD}{\angle BED} \tag{19}$$

Substituting the previous equation into the above equation, we can get that

$$2r_1 \sin\frac{\theta}{4}\cos\frac{\theta}{4} - \frac{\epsilon}{2} = 2r_2 \sin\frac{\phi}{4}\cos\left(\frac{\theta}{2} - \frac{\phi}{4}\right) \tag{20}$$

$$2\frac{W}{\theta}\sin\frac{\theta}{4}\cos\frac{\theta}{4} - \frac{\epsilon}{2} = 2\frac{W-\epsilon}{\phi}\sin\frac{\phi}{4}\cos\left(\frac{\theta}{2} - \frac{\phi}{4}\right) \tag{21}$$

The above equation is so complex that we cannot get an explicit function between θ and ϕ; however, we can plot their curve, as shown in Fig. 16. Obviously, $\theta<\phi$, and the curve b is discarded. The curve a shows that there is approximately linear relationship between θ and ϕ, i.e.,

$$\phi \approx k\theta \tag{22}$$

where $k = 2.102$ is a constant coefficient to fit the mapping from θ to ϕ.

APPENDIX B

Control sequence details

The control sequences utilized for various scenarios in the experimental tests are detailed in Table III. The robot achieves a maximum forward traveling velocity of 1.77BL/s at the control sequence T=[150, 150, 100, 250]ms, so we assume that T_1=150ms and T_3=100ms are suitable inflating intervals for the robot, and keep them constant during most experiments. Moreover, in terrestrial turning experiments, we assume that T_2 and T_4 follow the ratio of 150:250; therefore, the control sequences under various frequencies follow

$$T = [150, 0.375(\frac{1000}{f} - 250), 100, 0.625(\frac{1000}{f} - 250)] \tag{23}$$

where f=0.6~3.0Hz is the control frequency for the robot. Considering the control accuracy of MCU, T_2 and T_4 calculated by the above equation are rounded to obtain the final control sequence. The fastest turning velocity of 21.9°/s using the first mechanism happens at 1.2Hz, where T=[150, 219, 100, 365]ms; the fastest turning velocity of 111.8°/s using the second mechanism happens at 3.0Hz, where T=[150, 31, 100, 52]ms, as shown in Fig. 12(c).

During the multi-terrain experiments, except for the gap, the robot follows a specific control sequence T=[150, 150, 100, $*$]ms, where '$*$' indicates that the upper and lower chambers of the robot remain unactuated, waiting for the next command. In contrast, when the robot encounters a gap, it employs a different control sequence T=[50, 50, 50, 500]ms and crawls through the gap by wriggling. The robot demonstrates successful traversal across various substrates, such as glass, wood, carpet, sand, mud, and gravel, using a uniform control sequence T=[150, 281, 100, 469]ms. Notably, there is no requirement for individual parameter tuning specific to each substrate. However, when facing the transition between

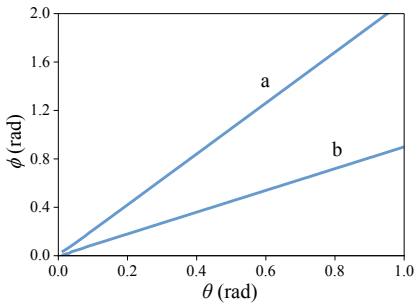

Fig. 16. Visualization of θ-ϕ mapping according to Equation (21).

TABLE III
CONTROL SEQUENCES UTILIZED FOR VARIOUS SCENARIOS IN THE EXPERIMENTAL TESTS.

	Motion	Control Sequence (ms)	Frequency (Hz)	Notes
Terrestrial Motions	Forward	[150, 150, 100, 250]	1.54	
	Backward	[0, 150, 100, 250]	2	
	Overturn	[250, 100, 100, 250]	1.43	
	Turning M_1	[150, 219, 100, 365]	1.2	
	Turning M_2	[150, 31, 100, 52]	3	Pre-curling actuated side for 300ms.
Aquatic Motions	Forward	[300, 0, 200, 100]	1.67	
	Backward	[150, 0, 200, 100]	2.22	
	Overturn	[300, 0, 200, 100]	1.67	
	Turning	[300, 0, 200, 100]	None	Pre-curling unactuated side for 300ms.
Multiple terrains	Slope	[150, 150, 100, $*$]	None	
	Obstacle	[150, 150, 100, $*$]	None	
	Single step	[150, 150, 100, $*$]	None	
	Continuous stairs	[150, 150, 100, $*$]	None	
	Gap	[50, 50, 50, 500]	1.54	
Various substrates	Glass	[150, 281, 100, 469]	1	
	Wood	[150, 281, 100, 469]	1	
	Carpet	[150, 281, 100, 469]	1	
	Sand	[150, 281, 100, 469]	1	
	Mud	[150, 281, 100, 469]	1	
	Gravel	[150, 281, 100, 469]	1	
Transitions	Water→land	[300, 0, 300, 0]→[300, 500, 150, $*$]	None	Switching when the robot body reach the black slope.
	Land→water	[150, 500, 100, $*$]→[300, 0, 200, 100]	None	Switching when the robot body reaches the blue water area.

1. '$*$' represents waiting for the next command, i.e., the robot executes the control sequence of T_1-T_3 and waits for the host computer to send the next command.
2. For a dual-body robot, only a single-side actuator is driven according to the control sequence during the turning process, while a pre-curling actuation is required before turning (see column of notes).

water and land, different control sequences are required and switched at the interface between the black slope and the blue water, as outlined in Table III.

REFERENCES

[1] R. M. Alexander, *Principles of animal locomotion*. Princeton University Press, 2003.

[2] R. Lock, S. Burgess, and R. Vaidyanathan, "Multi-modal locomotion: from animal to application," *Bioinspiration & Biomimetics*, vol. 9, no. 1, p. 011001, 2013.

[3] I. Delvolve, T. Bem, and J.-M. Cabelguen, "Epaxial and limb muscle activity during swimming and terrestrial stepping in the adult newt, pleurodeles waltl," *Journal of Neurophysiology*, vol. 78, no. 2, pp. 638–650, 1997.

[4] M. A. Ashley-Ross and B. F. Bechtel, "Kinematics of the transition between aquatic and terrestrial locomotion in the newt taricha torosa," *Journal of Experimental Biology*, vol. 207, no. 3, pp. 461–474, 2004.

[5] S. E. Peters, L. T. Kamel, and D. P. Bashor, "Hopping and swimming in the leopard frog, rana pipiens: I. step cycles and kinematics," *Journal of Morphology*, vol. 230, no. 1, pp. 1–16, 1996.

[6] A. Crespi, K. Karakasiliotis, A. Guignard, and A. J. Ijspeert, "Salamandra robotica ii: an amphibious robot to study salamander-like swimming and walking gaits," *IEEE Transactions on Robotics*, vol. 29, no. 2, pp. 308–320, 2013.

[7] R. Baines, S. K. Patiballa, J. Booth, L. Ramirez, T. Sipple, A. Garcia, F. Fish, and R. Kramer-Bottiglio, "Multi-environment robotic transitions through adaptive morphogenesis," *Nature*, vol. 610, no. 7931, pp. 283–289, 2022.

[8] Q. Ze, S. Wu, J. Dai, S. Leanza, G. Ikeda, P. C. Yang, G. Iaccarino, and R. R. Zhao, "Spinning-enabled wireless amphibious origami millirobot," *Nature Communications*, vol. 13, no. 1, p. 3118, 2022.

[9] J. Delmerico, S. Mintchev, A. Giusti, B. Gromov, K. Melo, T. Horvat, C. Cadena, M. Hutter, A. Ijspeert, D. Floreano *et al.*, "The current state and future outlook of rescue robotics," *Journal of Field Robotics*, vol. 36, no. 7, pp. 1171–1191, 2019.

[10] D. Wang, Y. Liu, J. Deng, S. Zhang, J. Li, W. Wang, J. Liu, W. Chen, Q. Quan, G. Liu *et al.*, "Miniature amphibious robot actuated by rigid-flexible hybrid vibration modules," *Advanced Science*, vol. 9, no. 29, p. 2203054, 2022.

[11] A. J. Ijspeert, A. Crespi, D. Ryczko, and J.-M. Cabelguen, "From swimming to walking with a salamander robot driven by a spinal cord model," *Science*, vol. 315, no. 5817, pp. 1416–1420, 2007.

[12] W. Wang, J. Yu, R. Ding, and M. Tan, "Bio-inspired design and realization of a novel multimode amphibious robot," in *2009 IEEE International Conference on Automation and Logistics*. IEEE, 2009, pp. 140–145.

[13] X. Liang, M. Xu, L. Xu, P. Liu, X. Ren, Z. Kong, J. Yang, and S. Zhang, "The amphihex: A novel amphibious robot with transformable leg-flipper composite propulsion mechanism," in *2012 IEEE/RSJ International Conference on Intelligent Robots and Systems*. IEEE, 2012, pp. 3667–3672.

[14] C. Kim, K. Lee, S. Ryu, and T. Seo, "Amphibious robot with self-rotating paddle-wheel mechanism," *IEEE/ASME Transactions on Mechatronics*, vol. 28, no. 4, pp. 1836–1843, 2023.

[15] A. Cohen and D. Zarrouk, "The amphistar high speed amphibious sprawl tuned robot: Design and experiments," in *2020 IEEE/RSJ International Conference on Intelligent Robots and Systems*. IEEE, 2020, pp. 6411–6418.

[16] R. Baines, F. Fish, and R. Kramer-Bottiglio, "Amphibious robotic propulsive mechanisms: current technologies and open challenges," *Bioinspired Sensing, Actuation, and Control in Underwater Soft Robotic Systems*, pp. 41–69, 2021.

[17] Z. Zhakypov and J. Paik, "Design methodology for constructing multi-material origami robots and machines," *IEEE Transactions on Robotics*, vol. 34, no. 1, pp. 151–165, 2018.

[18] D. K. Patel, X. Huang, Y. Luo, M. Mungekar, M. K. Jawed, L. Yao, and C. Majidi, "Highly dynamic bistable soft actuator for reconfigurable multimodal soft robots," *Advanced Materials Technologies*, vol. 8, no. 2, p. 2201259, 2023.

[19] H. Dong, H. Yang, S. Ding, T. Li, and H. Yu, "Bioinspired amphibious origami robot with body sensing for multimodal locomotion," *Soft Robotics*, vol. 9, no. 6, pp. 1198–1209, 2022.

[20] M. Wu, X. Xu, Q. Zhao, W. H. Afridi, N. Hou, R. H. Afridi, X. Zheng, C. Wang, and G. Xie, "A fully 3d-printed tortoise-inspired soft robot with terrains-adaptive and amphibious landing capabilities," *Advanced Materials Technologies*, vol. 7, no. 12, p. 2200536, 2022.

[21] J. Hwang and W. D. Wang, "Shape memory alloy-based soft amphibious robot capable of seal-inspired locomotion," *Advanced Materials Technologies*, vol. 7, no. 6, p. 2101153, 2022.

[22] D. P. Maitland, "Locomotion by jumping in the mediterranean fruit-fly larva ceratitis capitata," *Nature*, vol. 355, no. 6356, pp. 159–161, 1992.

[23] R. Bonduriansky, "Leaping behaviour and responses to moisture and sound in larvae of piophilid carrion flies," *The Canadian Entomologist*, vol. 134, no. 5, pp. 647–656, 2002.

[24] G. Farley, M. Wise, J. Harrison, G. Sutton, C. Kuo, and S. Patek, "Adhesive latching and legless leaping in small, worm-like insect larvae," *Journal of Experimental Biology*, vol. 222, no. 15, p. jeb201129, 2019.

[25] J. M. Newcomb, A. Sakurai, J. L. Lillvis, C. A. Gunaratne, and P. S. Katz, "Homology and homoplasy of swimming behaviors and neural circuits in the nudipleura (mollusca, gastropoda, opisthobranchia)," *Proceedings of the National Academy of Sciences*, vol. 109, no. supplement_1, pp. 10 669–10 676, 2012.

[26] Z. Zhou and R. Mittal, "Swimming without a spine: Computational modeling and analysis of the swimming hydrodynamics of the spanish dancer," *Bioinspiration & Biomimetics*, vol. 13, no. 1, p. 015001, 2017.

[27] N. geographic magazine, "What is this "red" creature dancing in the sea?" Video, 2020, accessed: January 24, 2024. [Online]. Available: https://www.youtube.com/watch?v=oUhBI8l2wiY

[28] S. Li, D. M. Vogt, D. Rus, and R. J. Wood, "Fluid-driven origami-inspired artificial muscles," *Proceedings of the National academy of Sciences*, vol. 114, no. 50, pp. 13 132–13 137, 2017.

[29] S. K. Mitchell, X. Wang, E. Acome, T. Martin, K. Ly, N. Kellaris, V. G. Venkata, and C. Keplinger, "An easy-to-implement toolkit to create versatile and high-performance hasel actuators for untethered soft robots," *Advanced Science*, vol. 6, no. 14, p. 1900178, 2019.

[30] A. A. Amiri Moghadam, S. Alaie, S. Deb Nath, M. Aghasizade Shaarbaf, J. K. Min, S. Dunham, and B. Mosadegh, "Laser cutting as a rapid method for fabricating thin soft pneumatic actuators and robots," *Soft Robotics*, vol. 5, no. 4, pp. 443–451, 2018.

[31] J. Fang, J. Yuan, M. Wang, L. Xiao, J. Yang, Z. Lin, P. Xu, and L. Hou, "Novel accordion-inspired foldable pneumatic actuators for knee assistive devices," *Soft Robotics*, vol. 7, no. 1, pp. 95–108, 2020.

[32] H. Jin, E. Dong, G. Alici, S. Mao, X. Min, C. Liu, K. Low, and J. Yang, "A starfish robot based on soft and smart modular structure (sms) actuated by sma wires," *Bioinspiration & Biomimetics*, vol. 11, no. 5, p. 056012, 2016.

[33] Y. Zhang, D. Yang, P. Yan, P. Zhou, J. Zou, and G. Gu, "Inchworm inspired multimodal soft robots with crawling, climbing, and transitioning locomotion," *IEEE Transactions on Robotics*, vol. 38, no. 3, pp. 1806–1819, 2021.

[34] E. Milana, B. Van Raemdonck, K. Cornelis, E. Dehaerne, J. De Clerck, Y. De Groof, T. De Vil, B. Gorissen, and D. Reynaerts, "Eelworm: A bioinspired multimodal amphibious soft robot," in *2020 3rd IEEE International Conference on Soft Robotics*. IEEE, 2020, pp. 766–771.

[35] T. Paschal, M. A. Bell, J. Sperry, S. Sieniewicz, R. J. Wood, and J. C. Weaver, "Design, fabrication, and characterization of an untethered amphibious sea urchin-inspired robot," *IEEE Robotics and Automation Letters*, vol. 4, no. 4, pp. 3348–3354, 2019.

[36] Y. Li, F. Fish, Y. Chen, T. Ren, and J. Zhou, "Bio-inspired robotic dog paddling: Kinematic and hydro-dynamic analysis," *Bioinspiration & Biomimetics*, vol. 14, no. 6, p. 066008, 2019.

[37] Y. Tang, Q. Zhang, G. Lin, and J. Yin, "Switchable adhesion actuator for amphibious climbing soft robot," *Soft Robotics*, vol. 5, no. 5, pp. 592–600, 2018.

[38] A. A. M. Faudzi, M. R. M. Razif, G. Endo, H. Nabae, and K. Suzumori, "Soft-amphibious robot using thin and soft mckibben actuator," in *2017 IEEE International Conference on Advanced Intelligent Mechatronics*. IEEE, 2017, pp. 981–986.

[39] D. Drotman, S. Jadhav, D. Sharp, C. Chan, and M. T. Tolley, "Electronics-free pneumatic circuits for controlling soft-legged robots," *Science Robotics*, vol. 6, no. 51, p. eaay2627, 2021.

[40] R. Chen, Z. Yuan, J. Guo, L. Bai, X. Zhu, F. Liu, H. Pu, L. Xin, Y. Peng, J. Luo *et al.*, "Legless soft robots capable of rapid, continuous, and steered jumping," *Nature Communications*, vol. 12, no. 1, p. 7028, 2021.

[41] T. Wang, H.-J. Joo, S. Song, W. Hu, C. Keplinger, and M. Sitti, "A versatile jellyfish-like robotic platform for effective underwater propulsion and manipulation," *Science Advances*, vol. 9, no. 15, p. eadg0292, 2023.

[42] J. Lee, Y. Yoon, H. Park, J. Choi, Y. Jung, S. H. Ko, and W.-H. Yeo, "Bioinspired soft robotic fish for wireless underwater control of gliding locomotion," *Advanced Intelligent Systems*, vol. 4, no. 7, p. 2100271, 2022.

Jiaxi Wu received the M.E. degree in control theory and control engineering from Institute of Automation, Chinese Academy of Sciences, Beijing, China, in 2022. He is currently working toward the Ph.D. degree with the College of Engineering, Peking University, Beijing, China.

His research interests include multi-modal soft robots, soft pneumatic actuator design, and soft robot locomotion control.

Mingxin Wu received the M.E. degree in Mechanical Engineering from Wuhan University, Wuhan, China, in 2020. He is currently working toward the Ph.D. degree with the College of Engineering, Peking University, Beijing, China.

His research interests include smart materials, robotic design, soft robotic grasping, and soft sensors.

Wenhui Chen received the M.E. degree in Materials Science from Wuhan University, Wuhan, China, in 2022. She is currently working toward the Ph.D. degree with the College of Engineering, Peking University, Beijing, China.

Her research interests include intelligent materials, soft robotics, and compliant mechanisms.

Chen Wang (Senior Member, IEEE) received the B.S. degree in electronic and information engineering from Xi'an Jiaotong University, Xi'an, China, in 2007 and her first Ph.D. degree in general mechanics and foundation of mechanics from Peking University, Beijing, China, in 2013. She received her second Ph.D. degree in systems and control from the University of Groningen, the Netherlands, in October 2014.

She is currently a Research Associate Professor in the National Engineering Research Center of Software Engineering, Peking University. Her research interests include biomimetic robotics, multiagent systems, and deep learning. She is an Associate Editor for *IEEE Robotics & Automation Magazine*.

Guangming Xie (Member, IEEE) received the B.S. degrees in applied mathematics and electronic and computer technology, the M.E. degree in control theory and control engineering, and the Ph.D. degree in control theory and control engineering from Tsinghua University, Beijing, China, in 1996, 1998, and 2001, respectively.

He is currently a Professor of Dynamics and Control with the College of Engineering, Peking University, Beijing. His research interests include smart swarm theory, biomimetic robots, and deep learning.